Probing the Plasmonic Near-Field of Gold Nanocrescent Antennas

Rostislav Bukasov,[†] Tamer A. Ali,[‡] Peter Nordlander,[‡] and Jennifer S. Shumaker-Parry[†,*]

[†]Department of Chemistry, University of Utah, 315 South 1400 East, RM 2020, Salt Lake City, Utah 84112, United States, and [‡]Department of Physics and Electrical and Computer Engineering, MS 51, Rice University, Houston, Texas 77005, United States

ABSTRACT We present an investigation of the plasmon-induced electromagnetic near-field around gold nanocrescent (NC) antennas which exhibit localized surface plasmon resonances (LSPRs) in the infrared. To probe the near-field behavior, we monitored the LSPR shift of NCs to adsorption of dielectric layers of varying thickness. The experimental results are analyzed using theoretical simulations, and the EM field decay lengths for the NCs are determined. We discuss how the structural properties of NC antennas influence the near-field properties and compare the results with the near-fields of other metal nanostructures. We show that the near-field distribution around NCs depends strongly on the structural parameters of the NC and that its spatial extent can be tuned to large distances (>700 nm) from the nanostructure surface. In addition, we discuss NC antenna structural changes associated with exposure to ethanol and buffer solutions and the impact on LSPR properties.

KEYWORDS: electromagnetic near-field · decay length · infrared plasmon · nanosphere template lithography · plasmonic nanostructure

Plasmonics as an interdisciplinary field involving light interaction with conductive matter on the subdiffraction limit length scale has attracted strong and increasing interest from the scientific community in the past decade.[1−5] Much of this attention concerns the application of nanoparticles in surface-enhanced spectroscopy[6,7] and sensing.[1,8,9] In addition, plasmonic interconnects and waveguides based on metal nanoparticle chains[10,11] and arrays[12] are expected to play a major role in the development of micro- and nanoscale optical devices.

The interaction of electromagnetic radiation with metal nanoparticles is the foundation of these applications and leads to the localized surface plasmon resonance (LSPR) phenomenon. One result of the excitation of plasmons is the creation of localized, enhanced electromagnetic (EM) fields, sometimes called hot spots. The EM near-field distribution on and near the surface of a metal nanoparticle is far from homogeneous, especially for anisotropic particles. This is particularly true for nanoparticles with sharp edges and, to a greater extent, sharp tips (vertices), which can spatially focus a significant portion of the incident EM field in an antenna effect.[13,14] The edges, tips, gaps, and similar features in asymmetric structures or in multiparticle assemblies such as dimers and other oligomers produce EM field hot spots where the local electric field amplitude can exceed the incident field by factors of 10 or greater ($E_{local}/E_{incident} \geq 10$).[15] For many plasmonic structures and multiparticle assemblies, simulations have predicted that local EM fields in hot spots may exceed the incoming field by 2 and even 3 orders of magnitude.[14,16]

Simulations also have predicted that the magnitude and degree of spatial localization of the plasmon-induced near-field vary significantly depending on the nanoparticle size, geometry, radius of curvature (*e.g.*, sharpness), and gap size between particles.[14,16] This dependence provides an opportunity to manipulate the behavior of local EM fields through structural control. The EM near-field tunability is essential for such applications as metal nanoparticle-based plasmon waveguiding,[17] LSPR sensing,[18] and surface-enhanced spectroscopies.[19] Maximum efficiency (*e.g.*, energy transfer, measured signal, or enhancement factor) would be achieved in these applications if the EM field could be focused into a well-defined volume depending on the application. For example, the decay length of the EM field near the metal nanoparticle surface determines the sensing depth for LSPR sensors. LSPR sensing is based on the shift of the LSPR wavelength, λ_{max}, upon binding of an analyte due to the change in dielectric environment near the

*Address correspondence to shumaker-parry@chem.utah.edu.

Received for review August 11, 2010 and accepted October 11, 2010.

Published online November 1, 2010. 10.1021/nn101994t

nanoparticle surface. The decay of the near-field determines the local probe volume and how far from a nanoparticle surface a binding event can be detected. The LSPR sensing depth was studied extensively for Au and Ag nanotriangle LSPR sensors by Van Duyne and co-workers.[18,20,21] They estimated an EM field decay length for Au nanotriangles of 5−15 nm (or 1−3% of light wavelength).[18] The effective sensing distance from the surface of Ag nanotriangles increased to up to 35 nm with a decrease in nanoparticle height from 40 to 25 nm.[9,18] For gold nanorings, Sutherland and co-workers estimated an EM field decay length of 12 nm (~1% of the wavelength), in agreement with discrete dipole approximation (DDA) calculations that predicted decay lengths in a range from 8 nm for the outer ring wall to 24 nm for the inner ring wall.[22]

Typically, the EM near-field decay lengths (~10 nm) for finite-size metal nanoparticles are an order of magnitude lower than for propagating surface plasmon polaritons excited in extended structures such as planar gold films (200−300 nm).[23,24] The short nanoparticle LSPR decay length has advantages and disadvantages depending on the intended application. The major advantage of a short decay length is a substantial red shift and high sensitivity to binding of small molecules near the surface (*e.g.*, small organic molecules and small proteins) and lower sensitivity to the bulk environment (*i.e.*, bulk refractive index changes, temperature fluctuations) beyond the local EM field.[22,25] A short decay length may be adequate for detection of the binding of two layers of medium-size protein molecules, such as streptavidin, so that the total multilayer thickness is well within 10 nm from the NP surface. However, the drawback of such a short decay length is that any adsorption events beyond the typical EM near-field decay length range are not detected. For instance, it would be difficult to detect the binding of large bioparticles such as viruses or bacteria to capture antibodies immobilized on the nanoparticle surface. A more extended sensing depth also is desirable for detection of binding events that do not take place directly on the plasmonic structure surface. With a more extended EM field decay length, it would be possible to detect adsorption events at a greater distance from the surface such as on a support layer covering the plasmonic structure. For example, a SiO_2 layer could be deposited on the plasmonic structures in order to create a platform for lipid bilayer assembly.[26] A more extended EM field decay, or longer-range sensing depth, would be necessary to then detect protein adsorption on this layer. Ideally, both the decay length as well as the LSPR wavelength should be tunable in order to optimize the plasmonic structures for specific sensing applications.

Nanocrescent (NC) antennas are one of the most structurally and optically tunable anisotropic metal nanoparticle morphologies.[27−30] The utility of the NCs' unique NIR and IR plasmonic tunability for surface-enhanced spectroscopy has already been demonstrated in the observation of one of the highest nanoparticle area normalized surface-enhanced infrared absorption spectroscopy (SEIRA) enhancement factors reported in the literature.[31] An understanding of how the NC structural parameters impact the EM near-field decay length is clearly important for LSPR sensing, light-guiding, and spectroscopy applications of NCs.

Kreiter and co-workers investigated the local field properties of NCs prepared using 200 nm diameter templates.[32] For those NCs with a low in-plane aspect ratio (*e.g.*, ratio of diameter to maximum width, 200/65 ≈ 3), they found that the LSPR shifts corresponded to EM field decay lengths of 26 and 17 nm from the NC surface for the two major dipole plasmon resonances. These decay lengths were about 1.5−3 times smaller than the theoretically predicted decay lengths obtained by assuming an exponential decay of the local EM field. Other authors have proposed that the LSPR probe length is related to the field intensity rather than the bare field, but so far, no conclusive proof for either has been presented.[18,33] The plasmon-induced intensity dependence is discussed in more detail later in this article. The same group reported a 20 nm probe depth near the tips of a 150 nm template diameter NC for the short-axis dipole resonance[32] but did not discuss the EM field behavior for any other region of the NC or for the dipole plasmon resonance excited along the long-axis of the NC.

In this paper, we present an investigation of the spatial distribution of the plasmon-induced near-field around gold NCs. To probe the near-field behavior, we monitored the LSPR shift of NCs to adsorption of dielectric layers of varying thickness. The experimental results are analyzed using theoretical simulations, and the EM field decay lengths for the NCs are determined. We discuss how the structural properties of NC antennas influence the near-field properties and compare the results with the near-field properties of other metal nanostructures. We show that the near-field distribution around NCs depends strongly on the structural parameters of the nanoparticle and that the spatial extent of the near-field can be tuned to large distances from the nanoparticle surface. The remarkable control of the spatial distribution of the near-field provided by NC suggests novel applications in plasmonic waveguiding and energy transfer applications.

RESULTS AND DISCUSSION

Nanocrescents are fabricated in large numbers (≈3 × 10^7 structures cm^{-2}) on a glass substrate with good control over size, shape, and orientation by nanosphere template lithography (NTL).[27,28] The NTL process starts with drop casting polystyrene (PS) beads on a glass substrate. The beads serve as individual templates for NC fabrication. Next, a gold film is deposited at a controlled

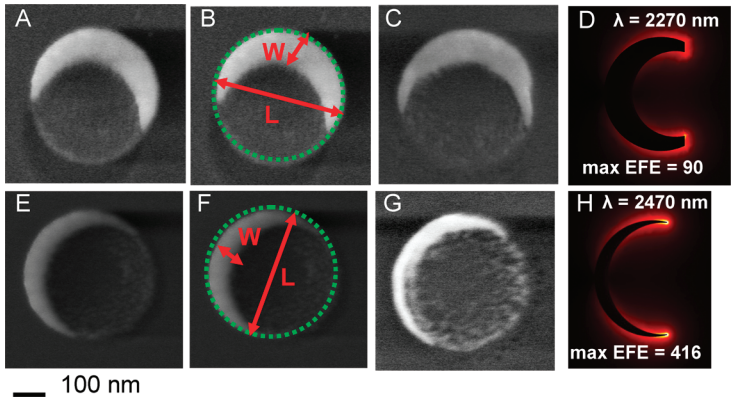

Figure 1. SEM images and local EM field maps of representative gold NC antennas prepared using 410 nm diameter templates. SEM images of (A) a low aspect ratio $NC_{10°}$, which was bare (*i.e.*, not coated with a SAM or proteins) and (E) a high aspect ratio $NC_{30°}$ coated with a BAT/OEG SAM before exposure to PBS buffer. The approach used to estimate the NC aspect ratios is shown in (B) and (F) where the aspect ratio is defined as the length/width (*L*/*W*) ratio. SEM images of NCs after exposure to PBS buffer (150 NaCl) show minimal structural changes for (C) a low aspect ratio $NC_{10°,PBS\ buffer}$ and more significant structure thinning for (G) a high aspect ratio $NC_{30°,PBS\ buffer}$ after exposure to PBS buffer. Calculated long-axis LSPR λ_{max} values and predicted EM fields for (D) a low aspect ratio NC and (H) a high aspect ratio NC. The NC subscripts indicate the angle used for NC fabrication and exposure to solvent prior to the measurement.

angle, and then this gold film is etched vertically with argon ion beam milling. Finally, the PS beads are removed from the substrate surface by lifting them off with tape. The result is an ensemble of mostly homogeneous individual NCs with uniform size and orientation, aspect ratio, and tip sharpness. The azimuthal deposition angle may be used to control the aspect ratio of the NCs. The azimuthal angle is the angle between the metal source in the evaporation chamber and the normal to the substrate mounted on the sample holder during metal film deposition. We define the NC aspect ratio as the ratio of the NC diameter to the NC width at a central point of the structure, as shown in Figure 1. A small azimuthal angle produces a thicker structure with a smaller in-plane aspect ratio, while larger angles result in a larger aspect ratio, more elongated and thinner NC. For example, an azimuthal angle of 10° produces NCs with an aspect ratio of about 4, as shown in Figure 1A. Thinner NCs with higher aspect ratios (5.5−6.6) are fabricated by using azimuthal deposition angles ranging from 25 to 35°. Throughout this article, we specify the angle of deposition *x*° as a subscript ($NC_{x°}$). Below we add a second subscript describing NC exposure to solvent. Figure 1E presents an example of a thinner, high aspect ratio $NC_{30°}$.

The extinction spectra presented in Figure 2 are representative for low and high aspect ratio NCs prepared using 410 nm diameter PS templates. The NCs have at least three well-separated, experimentally observed LSPR extinction peaks in the 600−3600 nm spectral range with two plasmon bands, the long-axis dipole resonance and short-axis dipole resonance, exhibiting high sensitivity to the dielectric environment.[27,31] We define the long-axis and short-axis resonances with respect to the NC antenna structure features, as shown in the inset in Figure 2. A third weak LSPR extinction peak on the blue side of the short-axis dipole in the NIR region is the long-axis quadrupole plasmon resonance. Since this mode has very small dipolar content, it couples only weakly to light. For the open NCs described in this paper, the quadrupole LSPR peak is in close proximity with the short-axis dipole LSPR peak and only occasionally appears in the spectra as a shoulder. Since this peak typically is not well-resolved, we do not discuss it further.

We used two experimental approaches to characterize the local EM fields for both high and low aspect ratio NCs. The first approach to probe the LSPR near-fields around the NC antenna on a nanometer-scale (<10 nm) is based on functionalizing the structures with a mixed self-assembled monolayer (SAM) containing biotin-terminated thiolates and then adsorbing streptavidin (SA) to form layers with fairly

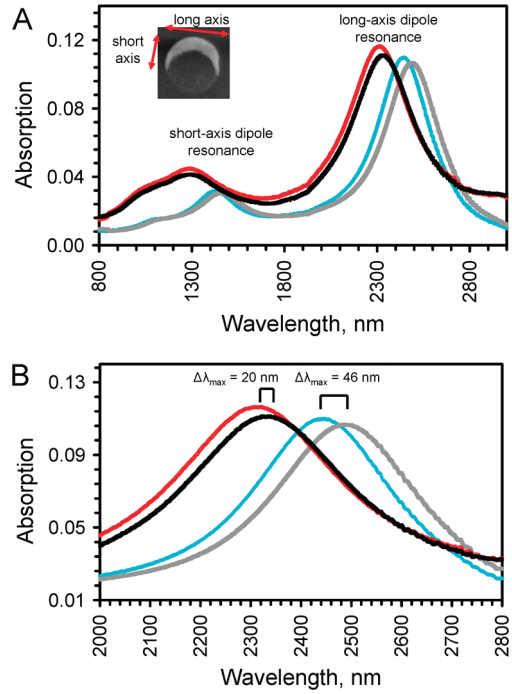

Figure 2. Representative vis−NIR extinction spectra of 410 nm template diameter NCs before and after streptavidin binding. (A) Spectra show LSPR peaks in a broad spectral range. (B) Magnified view of LSPR peaks from spectra in A. Red and turquoise spectra correspond to low aspect ratio structures ($NC_{10°}$) and high aspect ratio structures ($NC_{30°}$), respectively, after functionalization with a mixture of OEG- and BAT-terminated thiols. The high aspect ratio NCs ($NC_{30°,PBS\ buffer}$) were functionalized after exposure to PBS buffer. Black and gray spectra show the LSPR responses of the NCs after binding of streptavidin.

well-defined thicknesses. Upon the increase in the local refractive index of the medium near the surface of a NC due to binding of the SAM and the SA, the LSPR peak (λ_{max}) red shifts. We monitored these LSPR peak shifts ($\Delta\lambda_{max}$) after each adsorption step (the SAM and then the SA). In order to probe the decay of the near-field for larger distances, we deposited relatively thick (~18 nm) layers of silicon and monitored the LSPR $\Delta\lambda_{max}$ after deposition of each layer. The LSPR $\Delta\lambda_{max}$ response data from both experiments and calculations were used to estimate the plasmon EM near-field decay length for the NCs. As the position of the LSPR extinction peaks may vary over a broad spectral range depending on the NC structural parameters, we describe not only the absolute peak position shifts, $\Delta\lambda_{max}$, but also the relative LSPR shifts, $\Delta\lambda_{max}/\lambda_{max}$.[28]

NC Structural Changes Induced by Solvents. Prior to investigation of the EM near-field decay length, we observed structural changes after the NCs were exposed to solutions of PBS buffer or ethanol. The impact of the solvent exposure is most easily observed through blue shifts of the LSPR extinction peaks of NCs after exposure to these solvents. This blue shift is due to the rounding of the sharp NC tips. Similar structural changes upon exposure of gold and silver nanotriangles to solvents (including water) were reported by Van Duyne and coworkers.[25] Observation of similar solvent effects is not surprising given the fact that the nanotriangles are fabricated on a substrate using a nanosphere lithography process that is similar to the present NTL process used to prepare NCs. The experimentally measured blue LSPR shifts for the nanotriangles after exposure to solvents were supported by results from calculations by Hao *et al.*, which predicted a LSPR λ_{max} blue shift upon truncation of the tips of a nanotriangle.[34] Annealing of nanotriangles in ethanol and other solvents (*e.g.*, hexane, methanol) is typically used to saturate the structural changes after fabrication.[25,35]

We investigated the NC structural changes induced by solvent exposure. In particular, we probed if the effects of the structural changes on the LSPR measurements could be minimized by exposure of the NCs to solvents prior to any functionalization or adsorption process. Because ethanol is the solvent used for the SAM formation process, we first investigated the structural changes of NCs after exposure to ethanol. The NCs on glass were submerged in ethanol for 12−24 h. This exposure to ethanol resulted in blue LSPR λ_{max} shifts in the range of 5−12 nm (0.5−0.8% of $\Delta\lambda_{max}/\lambda_{max}$ relative shift) for the NCs. Those shifts are modest if compared to the 48 nm blue shift from 695 to 647 nm (7% of $\Delta\lambda_{max}/\lambda_{max}$ relative shift) for Ag nanotriangles after a 30 min exposure to water reported by Malinsky *et al.*[25] We found that, after 12 h of exposure to ethanol, the NCs were stable and did not undergo any further detectable structural or optical changes.

We also observed structural changes and LSPR λ_{max} shifts after exposure of the NCs to phosphate buffered saline (PBS). This was the same PBS buffer used for the SA adsorption experiments. When the NCs were immersed in the PBS buffer for a time comparable to that used for SA adsorption (~60 min), we observed λ_{max} shifts of ~10 nm, which were similar to the shifts observed after exposure to ethanol. However, we observed more significant structural changes when the NCs were exposed to the PBS buffer either by flowing the buffer over the NCs or when the NCs were immersed for a long period of time. After exposure of NCs to a flowing PBS solution, we observed significant λ_{max} blue shifts (*e.g.*, up to 87 nm) of the short- and long-axis dipole resonances and a decrease in the extinction amplitude. We also investigated the saturation of the spectral changes by monitoring the LSPR spectra after sequential exposures to PBS buffer until there was no shift or just a negligible blue shift in the LSPR λ_{max}. After 130 h of immersion of bare NCs in PBS solution, a saturation of structural changes was demonstrated by no further λ_{max} blue shift. The maximum total λ_{max} blue shift, which was observed for the long-axis dipole plasmon resonance, was about 110 nm. One possible explanation for the observed LSPR λ_{max} blue shift for the buffer-exposed NCs may be that the thickness of the NCs decreases due to etching induced by the presence of chloride ions (≈0.015 M of Cl^-) in the PBS buffer. Etching of the gold NCs could lead to an increase in the percentage of NC area exposed to the lower refractive index medium, air ($n \approx 1$), with a decrease of the area exposed to the glass substrate ($n \approx 1.6$), leading to more extensive blue shifts. Etching also will contribute to smoothing the NC structure and rounding its tips, leading to a larger blue shift. More detailed analysis of the NC structural changes and further investigation of this hypothesis is underway.

The experiments described above were done with unfunctionalized NCs. We also probed whether functionalization of the NCs with thiolates prior to PBS buffer exposure could protect the structures from the effects of the buffer. However, SAM-coated NCs still demonstrated a substantial blue shift of the λ_{max} in the range of 40−70 nm after immersion in PBS buffer for long periods of time. The most surprising finding was how the exposure to the buffer impacted the structure of SAM-modified NCs as shown by both the spectroscopic data and the SEM analysis. The SEM images of low aspect ratio NCs showed no detectable change in the maximum width or in-plane aspect ratio relative to NCs that were not exposed to buffer. However, after buffer exposure, the tips of the low aspect ratio NCs are rounded compared to the sharp tips typically observed for these structures, as shown in Figure 1A,C. In contrast, the SEM images of the high aspect ratio NCs exposed to PBS buffer demonstrated a decrease in the in-plane width (*e.g.*, by about half, typically from 70−90

TABLE 1. Summary of Relationship of Aspect Ratios of the NCs with Extinction Efficiency and LSPR Response to SA Binding

NC template diameter, angle of deposition, and etching process	aspect ratio	extinction efficiency	$\Delta\lambda_{max}$ (long axis)	$\Delta\lambda_{max}$ (short axis)
410 nm, 10°, PBS buffer	4.0	17[a]	12	7.5
410 nm, 30°, no exposure	6.6	29[a]	33	19
410 nm, 30°, PBS buffer	8.5	40[b]	43	37
291 nm, 30°, PBS buffer	6.2	29[b]	35	25

[a]Value was obtained using ~85% polarized light. [b]Value was obtained using 100% polarized light.

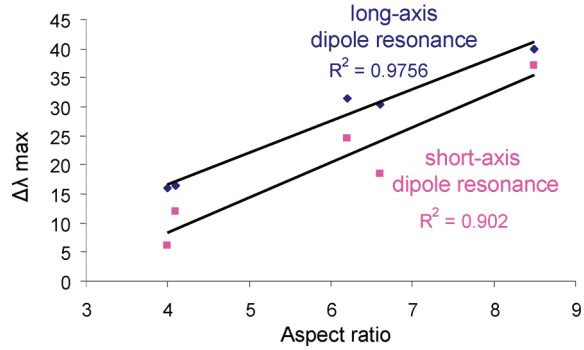

Figure 3. Long-axis and short-axis dipole LSPR λ_{max} shifts for 410 nm template diameter NCs upon streptavidin binding as a function of the NC in-plane aspect ratio.

nm to 33−50 nm for 410 nm NC template diameter) and a decrease in the radius of curvature of the NC tips (*i.e.*, increase in tip sharpness), as shown in the SEM images in Figure 1E,G. Those structural changes were accompanied by an increase in the aspect ratio from 6.6 to 8.5 and up to a 27% increase in NC extinction efficiency (from 29 to 40; see Table 1). The extinction efficiency, which is the ratio of optical cross section of a NC to its geometrical cross section, is an important parameter showing how efficiently a nanoparticle interacts with incident EM radiation. The overall extinction efficiency of a long-axis dipole LSPR peak is proportional to the NC in-plane aspect ratio as demonstrated in Figure 3. For 40 nm thick and 410 nm diameter NCs, which were exposed to PBS buffer (Figure 1G shows a representative SEM image), the extinction efficiency is as high as 40 if the spectrum is acquired with the incident light polarized along the long-axis of the NC. These NCs demonstrate the highest experimentally obtained extinction efficiency for any metal nanoparticle morphology reported in literature, demonstrating an unusually strong interaction of these structures with incident EM radiation.

We investigated the effect of the solvent-induced structural changes on the local EM fields using simulations. Figure 1D presents the EM field map for low aspect ratio NCs (AR = 4) and how the local field distribution may be impacted due to structural changes. From the simulations, the calculated extinction cross section of 2.2×10^{-12} m for a single NC with local EM field enhancement (*e.g.*, E_{local}/E_0, where E_{local} is the local EM field and E_0 is the incident EM field) is 90 near the NC tips. On the basis of this optical cross section as well as on an estimate of the NC geometrical cross section (0.057 μm^2), the structure has an extinction efficiency about 40.[28] This number is approximately twice the experimental extinction efficiency of low aspect ratio NCs. The simulation of the local electric field on and near the high aspect ratio NC produced an extinction cross section of 1.9×10^{-12} m for a long-axis dipole mode of a single NC with local electric field enhancement as high as 400 near the NC tips, as shown in Figure 1H. On the basis of this optical cross section as well as on an estimate of the NC geometrical cross section (0.025 μm^2), the NC extinction efficiency is estimated to be 76. To our knowledge, this value is the highest calculated extinction efficiency reported for any nanoparticle morphology. This number is again about twice the experimental value for ensemble measurements for the high aspect ratio NCs. A possible explanation for the difference between the experimental and calculated values may be the effect of the EM field interference from neighboring NCs in the ensemble. Also, structural imperfections such as surface roughness that are not accounted for in the model but are present in the experimental NC structures may contribute to this difference in extinction efficiency.

More detailed characterization of the observed LSPR λ_{max} blue shift upon exposure of NCs to different solvents will be discussed in a future publication. However, in all cases, when we exposed NCs to different solvents and solutions, only blue shifts in NC extinction spectra were observed. Therefore, we may assume that, upon functionalization of NCs with SAMs, the red shift upon SAM formation will not overestimate the response of the NCs to the SAM layer. On the contrary, the LSPR λ_{max} red shift upon SAM formation on the NC may be somewhat diminished and therefore underestimated if there is a simultaneous blue shift due to solvent effects. However, unless specifically noted, we may disregard the solvent effects after SAM or SA binding. This is in part because the solvent effects had been saturated for most of the samples included in the data analysis. In addition, the PBS buffer exposure time was relatively short (60−100 min) compared to the saturation immersion time (12+ hours) which led to the largest structural changes and blue shifts, and therefore, the effects of solvent exposure on the LSPR λ_{max} shifts are expected to be minimal even in the presence of NaCl. In order to provide complete information about the NC samples, we include an additional subscript, $NC_{x°,solvent}$ to indicate exposure to PBS buffer or ethanol prior to functionalization. If there was no exposure of the NCs to solvent prior to the functionalization or measurement, no solvent subscript is included. The first subscript, $x°$, is the

deposition angle used in the fabrication of the NCs as described above.

Probing the Response of NCs to Adsorption of Thin Dielectric Layers. We used SAM formation of ω-functionalized alkyl thiols and streptavidin (SA) adsorption to characterize the short-range EM field decay near NC antennas. A mixed SAM containing biotin- and oligo(ethyleneglycol)-functionalized alkyl thiols (BAT and OEG, respectively) was used to provide a binding surface for SA adsorption. For these studies, we allowed the SAM to form from a mixed BAT/OEG solution in ethanol for 2 h and observed NC λ_{max} red shifts in a range of 5−13 nm. After SAM formation, we exposed the NCs to SA, which was expected to bind to the biotin groups exposed on the SAM-functionalized NC surface. In the characterization of the short-range EM near-field decay, the LSPR peak in the visible spectral region was not analyzed because the LSPR peak shifts upon SAM formation and SA binding were modest (only a few nanometers) and in fact close to the uncertainty of the λ_{max} measurement (*e.g.*, 0.5−2 nm depending on the LSPR peak width and amplitude). The measured average red shifts or $\Delta\lambda_{max}$ values were 8−37 nm for the short-axis dipole and 17−40 nm for the long-axis dipole LSPR peaks, depending on the aspect ratio of the NCs. Results for representative NC samples are summarized in Table 1. For the 410 nm template diameter NCs, we observed increases in the red shifts of both the long-axis and short-axis dipole plasmon resonances with an increase in the NC aspect ratio. Values of $\Delta\lambda_{max}$ for SA binding increased by an average of ~85% when the in-plane aspect ratio of NCs increased from about 4 for the low aspect ratio structures ($NC_{10°}$) to an average of 6.6 for high aspect ratio structures ($NC_{30°}$). The magnitude of the LSPR shift is larger than that observed for the low aspect ratio NCs ($NC_{10°}$) by as much as 110% for the thinnest NCs ($NC_{30°,PBS\ buffer}$) with an aspect ratio of 8.5, which were the results of exposing thin, high aspect ratio NCs ($NC_{30°}$) to PBS buffer. Figure 3 presents the linear dependence of the $\Delta\lambda_{max}$ for long-axis and short-axis dipole resonances on aspect ratio for some representative NC samples. For the thin NCs fabricated with a 30° azimuthal angle ($NC_{30°}$), the initial in-plane aspect ratio is 6.6, which increased by 29% to 8.5 upon exposure to the PBS buffer ($NC_{30°,PBS\ buffer}$). This increase is very well matched by about the same $\Delta\lambda_{max}$ increase of 30% for the long-axis plasmon resonance from 33 to 43 nm.

For the thicker, lower aspect ratio AuNCs (*i.e.*, $NC_{10°}$) that had no measurable change in aspect ratio after exposure to solvents, there is no increase in the long-axis dipole LSPR $\Delta\lambda_{max}$ but a decrease in the short-axis LSPR $\Delta\lambda_{max}$ from 12−15 to 8 nm that may be due to a slight truncation of the tips of the structures (Figure 2B). For SA binding to the thin 410 nm diameter NCs formed by exposure to PBS (*i.e.*, $NC_{30°,PBS\ buffer}$) and then functionalized with a BAT/OEG mixed SAM, we observed up to a 43 nm long-axis LSPR λ_{max} red shift from 2445 to 2485 nm (a relative shift ($\Delta\lambda_{max}/\lambda_{max}$) of 1.8%) as well as up to a 37 nm short-axis λ_{max} red shift from 1425 to 1462 nm (2.5%). Both of these shifts are larger than the 27 nm λ_{max} red shift (*e.g.*, 3.8% relative shift) reported for SA binding to biotin-functionalized Ag nanotriangular prisms with LSPR λ_{max} of 610 nm.[36] Also, both AuNC LSPR red shifts are much larger than the absolute and relative red shifts for bovine serum albumin ($\Delta\lambda_{max}$ = 6.4−13.4 nm or 1.2% relative shift) and neutravidin ($\Delta\lambda_{max}$ = 3.7 nm or 0.3% relative shift) binding to a gold nanoring-based LSPR sensor with an LSPR λ_{max} of about 1120 nm.[22] The larger LSPR response is not surprising due to the increase in the refractive index sensitivity of the NC antennas which have LSPRs at longer wavelengths compared to the nanotriangles and nanorings.[28] The distribution of the local EM fields near the surfaces of these different plasmonic structures also plays a role. This is demonstrated by the dependence of the LSPR response ($\Delta\lambda_{max}$) on the aspect ratio of the NCs.

Overall, we found that the structural changes induced by exposure of the NCs to solvent such as PBS buffer containing NaCl may be useful in tailoring the properties of the structures. For example, our investigations show that the thinner, high aspect ratio NCs are more sensitive to the local dielectric environment in the distance range of <10 nm than any other LSPR sensor based on other NP morphologies, in terms of the absolute $\Delta\lambda_{max}$ response. In general, thinner, higher aspect ratio NCs provide higher sensitivity compared to lower aspect ratio structures for binding of small- and medium-sized molecules to the SAM-functionalized NC surface.

Investigation of the Longer-Range NC EM Field Decay Using Silicon Layers. In order to probe the EM near-field for larger distances, we coated NCs with multiple layers of amorphous silicon by sputtering. We prepared the coated NCs in a stepwise approach and measured the NC LSPR λ_{max} shift ($\Delta\lambda_{max}$) after addition of each layer. We used SEM images of the NC structures to develop models for calculating the LSPR response to layers of dielectric material. We combined the experimental and calculated LSPR response data to estimate the decay lengths for the long-axis and short-axis plasmon resonances. This is described in more detail below.

Low and high aspect ratio 410 nm AuNCs were coated with up to 55.2 nm of silicon in three 18.4 ± 1.5 nm thick layers by sputtering. LSPR extinction spectra were collected after deposition of each silicon layer. Significant LSPR λ_{max} red shifts were observed after each deposition step for both dipolar NC LSPR modes, as shown by the representative spectra in Figure 4. The red shift for each of the plasmon resonances exceeds the uncertainty in the λ_{max} measurement (*e.g.*, 2−4 nm for λ_{max}= 2200−3300 nm) by at least 1 or even 2 orders of magnitude. As expected, with each additional layer

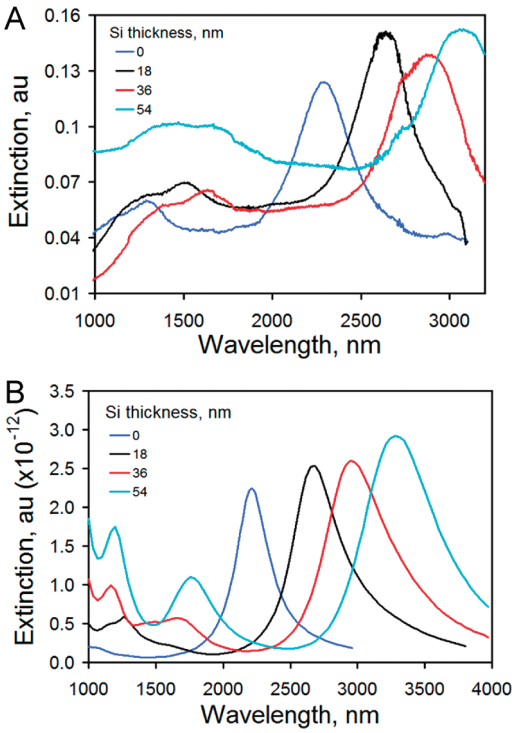

Figure 4. (A) Experimental ensemble LSPR extinction spectra and (B) simulated single-particle NC extinction spectra for 410 nm template gold NCs and after coating with three 18 nm thick silicon layers.

of silicon, the LSPR peaks red shift. For thicker silicon layers, the individual LSPR peaks were difficult to distinguish due to additional structure in the spectra, most likely due to additional scattering and Fabry−Perot (FP) resonances in the silicon layer. We calculated the extinction spectra of an individual gold NC on a glass substrate with the same inner diameter (410 nm) and structural characteristics as the fabricated NCs. Figure 4 presents the calculated spectra for a bare NC and for the same structure after sequentially adding 18 nm thick silicon layers. The values for both the experimental spectra and the calculated spectra are shown in Table 2. There is excellent agreement between the LSPR λ_{max} values from the experiment and the simulation for bare NCs and after adding silicon layers, especially considering that the model does not take into account some the structural features such as grain size and roughness. The similarity between the measured and calculated LSPR widths is additional evidence for the homogeneity of the NCs in the ensemble-based experimental measurements.

TABLE 2. NC Extinction Peak λ_{max} for Long-Axis and Short-Axis Dipole LSPRs Obtained from Experiment and Simulation after Addition of Silicon Layers

	long-axis dipole λ_{max}, nm		short-axis dipole λ_{max}, nm	
silicon layer thickness, nm	experiment	simulation	experiment	simulation
0	2290	2270	1300	1300
18	2640	2620	1516	1550
36	2875	2900	1642	1630
54	3129	3170	1706	1700

We used the experimental and simulation data of the LSPR response of the NCs to the addition of silicon layers to estimate the LSPR EM near-field decay length. In contrast to propagating plasmons in a planar geometry where the near-field decays exponentially away from the surface, the local fields around a finite nanoparticle will decay polynomially.[37] However, the near-field around a finite nanoparticle can be approximately parametrized using an exponential decay.[18,20,21,33,37] For simplicity, we therefore apply the relationship used by Jung *et al.*[23] to describe the EM field of a propagating plasmon at a planar gold film−dielectric interface as follows

$$\Delta\lambda_{max}(d) = m(n_a - n_s)\left[1 - \exp\left(\frac{-2d}{l_d}\right)\right] \quad (1)$$

where $\Delta\lambda_{max}(d)$ is the SPR wavelength shift response to the addition of a dielectric layer with thickness d, m is the sensitivity of the SPR sensor to bulk refractive index changes, n_a is the refractive index of the adsorbed layer, n_s is the refractive index of the medium of the bulk or surrounding dielectric material, and l_d is the EM near-field decay length. Several groups have used this relationship to describe the EM near-field decay for finite plasmonic metal nanostructures.[18,21,33] For an anisotropic metal nanostructure, this relationship is an oversimplification. This is certainly the case for NCs where simulations predict a strong directional dependence of the EM field decay on the local structural properties. Although eq 1 does not take into account the anisotropy of the EM near-field, the single exponential can be used to provide an approximation of the average field decay, which is what is probed in our experimental measurements.

We have used eq 1 to estimate the decay length for the 410 nm NCs. Two approaches may be used to apply eq 1. The first is to measure the sensitivity factor, m, for the NCs and incorporate the refractive indices for bulk dielectric material, which is air ($n_s = 1.00$), for our measurements and the dielectric of the silicon layers ($n_a = 3.46$ at the LSPR wavelengths probed in the experiment). A disadvantage with this approach is that it is rather tedious to measure m at multiple wavelengths across the entire LSPR wavelength region for different solvents with known n values and no absorption bands which would interfere with the LSPR shift measurements. An alternative approach is to use the fact that the term $m(n_a - n_s)$ describes the maximum NC LSPR response expected for an infinitely thick adsorbed layer of material with a refractive index of n_a. We can then measure the maximum LSPR response at saturation, $\Delta\lambda_{max}(d_{sat})$. This would normally be done by monitoring the LSPR λ_{max} shift for thicker layers of the material (*e.g.*, silicon for these experiments) until there is no ad-

TABLE 3. Optical Properties of NCs, Nanorings, and Nanotriangles

morphology	type of resonance	LSPR λ_{max}, nm	probe depth, nm	decay length, nm	relative decay length, %	source
crescents	long-axis dipole	3170	346	692	22	experiment
crescents	long-axis dipole	3129	370	740	24	simulation
crescents	short-axis dipole	1700	252	404	24	experiment
crescents	short-axis dipole	1796	217	434	24	simulation
crescents[32]	long-axis dipole	1364	26.2[a]	52[a]	4	experiment
crescents[32]	long-axis dipole	1364	70[a]	140[a]	10	simulation
crescents[32]	short-axis dipole	897	17.2[a]	34.4[a]	4	experiment
crescents[32]	short-axis dipole	897	32[a]	64[a]	7	simulation
nanorings[22]	in-plane dipole	1100		12[b]	1	experiment
nanotriangles[18]	in-plane dipole	700		5−15[c]	1−3	experiment

[a]Values were adjusted to take into account the light intensity dependence related to the square of the local field. [b]Decay length values were found using an approach taking into account the light intensity dependence of the measured LSPR response. [c]Decay length values were taken from the summary by the authors.

ditional LSPR λ_{max} shift indicating saturation. However, we found that the experimental measurement of the saturation of $\Delta\lambda_{max}(d_{sat})$ presents a challenge due to the spectral changes caused by the FP resonances. As an alternative, we used simulations to estimate the saturation LSPR $\Delta\lambda_{max}$ for the NCs.

In order to estimate the EM field decay length, we replace $m(n_a - n_s)$ with $\Delta\lambda_{max}(d_{sat})$. As mentioned above, the maximum LSPR $\Delta\lambda_{max}(d_{sat})$ is the LSPR peak shift after which there is no additional shift with an increase in the thickness of the dielectric layer (in this case silicon) covering the NC. After replacing $m(n_a - n_s)$ with $\Delta\lambda_{max}(d_{sat})$ and rearranging the terms, eq 1 takes the form

$$1 - \frac{\Delta\lambda_{max}(d)}{\Delta\lambda_{max}(d_{sat})} = \exp\left(-\frac{2d}{l_d}\right) \quad (2)$$

We linearized this relationship and used experimental and calculated values for $\Delta\lambda_{max}(d)$ for a range of silicon layer thicknesses (d = 0, 18, 36, 54 nm) to estimate the average decay length, l_d. Simulations provided values for $\Delta\lambda_{max}(d_{sat})$ of 6330 and 2300 nm for the long-axis LSPR and the short-axis LSPR, respectively. The silicon layer thickness that produced these saturation LSPR $\Delta\lambda_{max}(d_{sat})$ values was 400 nm. The estimated decay lengths are presented in Table 3. We also include the decay lengths for smaller NCs, nanotriangles, and nanorings which were all fabricated using a template lithography process on a substrate. The NC data published by Bocchio *et al.*[32] also were based on application of an exponential relationship to estimate the decay length for smaller NCs. However, we adjusted the value for the EM near-field decay length to take into account the dependence on the local field intensity to allow direct comparison of data for all of the structures. This dependence on intensity, or E_{local}^2, is incorporated in eqs 1 and 2 by including the factor of 2 in the exponent. The values provided by Bocchio *et al.*[32] more accurately describe the probe depth, which is one-half of the field decay length. The local field intensity is especially important to consider due to the dependence of refractive index sensing and spectroscopy applications on the local light intensity.

The long-axis LSPR decay lengths of 692 nm (experimental) and 740 nm (simulation) and the short-axis decay lengths of 404 nm (experimental) and 434 nm (simulation) significantly exceed both the predicted and measured EM field decay lengths for other fabricated structures such as gold nanotriangles (~12 nm) and gold nanorings (5−15 nm). The decay length values for the 410 nm template NCs also exceed both experimental (52 nm) and simulated (140 nm) decay lengths for low aspect ratio (AR = 3) NCs of smaller template diameter (200 nm).[32] Overall, longer field decay lengths for the larger NCs are expected due to the much longer wavelengths of the LSPRs compared to the plasmon resonances for smaller NCs, nanotriangles, and nanorings. In order to compare the behavior for different structures, normalization of the EM field decay length to either nanoparticle size or LSPR wavelength is one approach to assess how the EM decay length varies for a given geometry relative to the decay length for other geometries. We therefore normalized the EM near-field decay length to the wavelength of the LSPR. This is especially useful in situations where the exact geometry of the particle cannot be unambiguously determined. For example, two NC samples of the same template diameter but different aspect ratios (fabricated at different azimuthal metal deposition angles) would have different LSPR λ_{max} values and EM near field behavior. Such a ratio of the decay length to the LSPR λ_{max} was also used in the characterization of the LSPR EM field decay near Ag nanotriangles by Haes *et al.*[18]

Relative decay lengths obtained from both experiments and simulations for the 410 nm templated NCs, as well as for the smaller NCs, nanotriangles, and nanorings are presented in Table 3. In addition to exhibiting significantly larger absolute decay lengths, the NCs also have larger relative decay lengths (22−24% relative to the LSPR wavelength) compared to the other structures. The more extended EM near-field decay for the larger NCs is

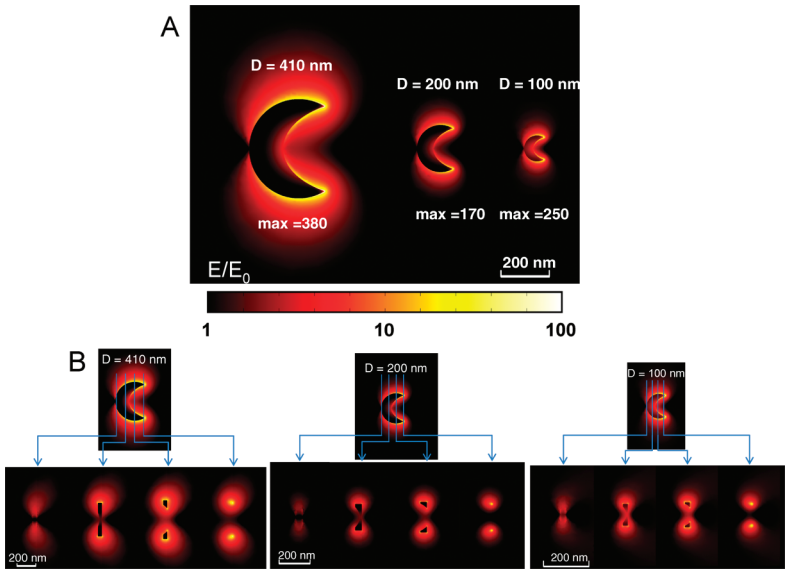

Figure 5. (A) Calculated near-field distributions for excitation of the longitudinal dipolar resonance of three NCs of different template diameter (*D*) and structure thickness (*T*) at resonance (λ_{max}): $D = 410$ nm, $T = 43$ nm at $\lambda_{max} = 2200$ nm; $D = 200$ nm, $T = 43$ nm at $\lambda_{max} = 1500$ nm; and $D = 100$ nm and $T = 20$ nm at $\lambda_{max} = 1200$ nm. (B) Near-field distribution in vertical sections perpendicular to the NC plane for the NCs in (A).

surprising based on the behavior of the smaller NCs. One would expect the relative decay lengths to be quite similar. These results show that the EM field decay length does not scale simply with nanoparticle size and LSPR wavelength. Instead, there seems to be a transition where the EM fields become much more extended, such as in the case of the larger NCs.

Evidence for this transition is shown in Figure 5, where the plasmon-induced near-field is shown for three NC of different sizes. For the large NC in Figure 5A, the near-field extends more than 400 nm away from the tips in the longitudinal direction, while for the two smaller structures in Figure 5B,C, it is much more confined. Interestingly, the smaller 210 nm templated NCs exhibit relative decay lengths (4−10%), which are between the results for the nanotriangles (1−3%) and nanorings (1%) and the more extended fields and much larger relative decay (22−24%) of the 410 nm templated NCs. The different relative decay lengths for the 410 and 210 nm templated NCs demonstrate the possibility of controlling and manipulating the near-fields around the NC within a large spatial range. Although the amplitude of the field diminishes over the decay length, less localized fields may be useful in some applications. For example, the much more extended EM fields of the 410 nm templated NCs provide an opportunity to transfer energy over longer distances and an opportunity for coupling of the EM fields to surrounding materials. Our estimated decay lengths of the plasmon-induced near-field should not be taken literally due to the assumption of an exponential decay in the model (eqs 1 and 2). However, the finding of the significantly extended decay lengths for the larger NCs clearly reflects the physical situation as also illustrated in Figure 5. A more detailed investigation of how the near-field distribution is influenced by the structural parameters of the NC will be presented in a future publication.

CONCLUSION

The distribution of EM near-fields on and near the surface of plasmonic structures is important for a wide range of applications. Ideally, the EM near-field decay length would be tunable in order to optimize plasmonic materials for particular applications such as EM energy transfer and near-field coupling between adjacent metal nanoparticles in plasmonic waveguide applications and tailoring of the probe depth and signal enhancements for sensing and spectroscopy applications. Nanocrescent antennas demonstrate much more extended EM field decay lengths compared to other nanostructures prepared by nanosphere templating methods. The relative plasmon near-field decay lengths of the larger 410 nm templated NCs (22−24%) of higher aspect ratio (AR = 4−8.5) are much larger than that of smaller 210 nm templated NCs (4−10%) of lower aspect ratio (AR = 3). This demonstrates the possibility of tuning the near-field decay over a large range of distances from the surface of the nanostructures. Future investigations will focus on obtaining a three-dimensional map of the spatial distribution of the EM fields for a wide range of NC antenna structures.

More detailed characterization of how lithographically produced plasmonic structures are impacted by exposure to a range of solvents is needed to better understand how structures may hold up for applications which involve solvents. NC antennas demonstrate small structural changes, mostly observed by LSPR shifts, upon exposure to ethanol. However, exposing NCs to PBS buffer containing NaCl leads to much larger structural changes for some NCs, and the apparent etching seems to depend on the NC aspect ratio. Thinner, high aspect ratio NCs were more impacted by exposure to PBS buffer than lower aspect ratio NCs. More studies must be done to fully understand solvent-induced structural changes, but overall, the impact for NCs is minimal over short (hours) exposure times.

We also demonstrate that by controlling the NC aspect ratio, the sensitivity to adsorption of thin dielectric layers and the structure extinction efficiency may be tuned. Thinner NCs with aspect ratios above 8.5 ex-

hibit the largest reported experimental and calculated nanoparticle extinction efficiencies of 40 and 78, respectively. Upon fabrication of thinner, higher aspect ratio NCs, an even higher extinction efficiency and a higher LSPR sensitivity to adsorption of thin dielectric layers would be expected. The higher aspect ratio NCs may be fabricated simply by adjusting the azimuthal angle used during the metal deposition process.

EXPERIMENTAL MATERIALS AND METHODS

Materials. Au pellets (99.999%) were purchased from K. J. Lesker (Philadelphia, PA). Polybead polystyrene microspheres and polystyrene NIST particle size standards were purchased from Polysciences, Inc. (Warrington, PA). Coverslips were purchased from Ted Pella (Redding, CA). Carbon disulfide was purchased from Fisher Chemicals, and anhydrous carbon tetrachloride was purchased from Sigma-Aldrich. For all steps of substrate preparation, we used water purified to 18 MΩ using a NANOpure Dlamond system from Barnstead. Absolute ethanol (200 proof) was obtained from Aaper (Shelbyville, KY). (1-Mercapto-11-undecyl)tetra(ethylene glycol) (OEG) and biotin-terminated tri(ethylene glycol)hexadecanethiol (BAT) were purchased from Asemblon (Redmond, WA). Immunopure streptavidin (SA) was used as received from Pierce (Rockford, IL). Phosphate buffered saline (PBS, 150 mM NaCl) was prepared in the laboratory by dissolving 8 g of NaCl, 0.2 g of KCl, 1.44 g of Na_2HPO_4, and 0.24 g of KH_2PO_4 in 1000 mL of deionized water, with pH adjusted to 7.4 by addition of several drops of HCl.

Methods. Glass substrates were cleaned by immersion in piranha solution (7:3 volume ratio of H_2SO_4/30% H_2O_2) for 30 min (WARNING: Piranha solution is very corrosive and must be handled with extreme caution; it reacts violently with organic materials and may not be stored in tightly closed vessels). The substrates were rinsed repeatedly in nanopure water and then sonicated in 5:1:1 volume ratio H_2O/NH_4OH/30% H_2O_2 solution at 50 °C for 1 h. After copious rinsing with water following sonication, substrates were used immediately or stored in nanopure water for no longer than one week.

Nanocrescents were fabricated using a nanosphere template lithography (NTL) process. The first step of NTL is to deposit polystyrene (PS) beads on a glass coverslip with submonolayer coverage. Colloid solutions stored at 4 °C were allowed to warm to room temperature. A volume of the solution was diluted in absolute ethanol, so the resulting solution would provide a substrate surface coverage of about 2−3% of a monolayer of beads. For example, a dilution of 1:60 was used for the 410 nm colloid solution. After cleaning, the substrates were rinsed in ethanol and dried in a stream of nitrogen. A 15 μL aliquot of polystyrene colloid solution was deposited on the substrate surface. After 20−30 s, the substrates were dried individually using nitrogen flow. The drying procedure is critical to ensure the maximum uniformity of colloid distribution and to prevent the formation of close-packed agglomerates. Dark-field microscopy (Nikon Eclipse TE-2000U) was used to examine the dispersion of the PS spheres on the substrate. PS sphere-coated substrates were mounted on custom holders, which allowed tilt angles of θ = 20 or 40° to control the deposition angle, which is the key element of the second step in the fabrication, as shown in Figure 1. Those substrate holders were installed on carrier rails inside an electron-beam evaporator chamber. By varying the second holder's position on the carrier rails, the azimuthal angle with respect to the source also could be adjusted. Gold was deposited using an electron-beam evaporator (Denton Vacuum USA, Moorestown, NJ). The metal film thickness and deposition rate (1 Å/s) were measured with a quartz crystal microbalance (XPC2, Inficon, East Syracuse, NY). As shown in Figure 1, step 3, an argon ion milling system (Plasmalab 80 Plus, Oxford Instruments) was used to remove the gold film not protected by the PS spheres. PS spheres were lifted off the substrate by the application of transparent tape (Magic Tape, 3M).

The NCs were exposed to a mixture of BAT (0.09 mmol/L) and OEG (0.9 mmol/L) in ethanol for 2 h. The second component was used in 10:1 excess to generate a stable monolayer resistant to nonspecific adsorption of the streptavidin onto the gold surface of the AuNCs.[38] After collecting extinction spectra, we exposed those NCs to streptavidin solution (0.04 mg/mL or 0.75 μM) in PBS buffer for 2 h. Some uncoated (*i.e.*, no SAM) gold NCs were exposed to PBS buffer by submerging the samples in a beaker with flowing PBS solution added at 0.6−1 mL/min rate flow for 90 min. Each sample was copiously rinsed after exposure to solution with ethanol (after thiols) or with nanopure deionized water (after streptavidin and buffer) and dried in a nitrogen flow.

For the experiments using dielectric layers, freshly fabricated 410 nm AuNCs were coated with up to 55.2 nm of silicon in three 18.4 ± 1.5 nm steps by sputtering using a Denton Discovery 18 Sputter system from Denton Vacuum (Moorestown, NJ). LSPR extinction spectra were collected after each deposition. To determine the sputtering rate, a Tencor P-10 profilometer from KLA-Tencor (Milpitas, CA) was used to measure the thickness of silicon layers deposited on a bare glass substrate. The deposited thickness of silicon on the AuNC samples was also measured using the profilometer. This was done by including two pieces of vacuum tape on the corners of the NC substrate during silicon deposition. The tape was removed after the deposition of the first and the third layers of Si. The profile depressions in those bare areas previously occupied by the tape were in good agreement with the calculated sputtering rate.

The optical properties of the NCs were characterized by transmission vis−NIR spectroscopy and transmission FTIR spectroscopy. Extinction spectra were measured over a wavelength range of 500−3200 nm with a Perkin-Elmer Lambda 9 UV/vis/NIR spectrophotometer with light predominantly (~80%) polarized in the horizontal plane. Extinction represents a measure of the loss of light due to scattering, and absorbance and is defined as $E = (1 - I/I_0)$, where I_0 is the intensity of the incident light and I is the measured light intensity after the beam passes through the sample. Extinction spectra also were measured over a wavelength range of 2500−4000 nm with a Perkin-Elmer Spectrum 100 FT-IR spectrometer with randomly polarized light. In addition to those instruments, we used a Perkin-Elmer Lambda 750 UV/vis spectrometer with 100% angular controlled uniformly s-polarized light. The NC extinction efficiency was calculated from the spectroscopy data and electron microscopy analysis as described previously.[28]

A pair of glass cuvettes (10 mm path length, Perkin-Elmer) was used for extinction measurements in ethanol, CCl_4, and CS_2. An Abbe-3L refractometer was used to measure the refractive index of the solvents. Scanning electron microscopy (SEM, Philips XL 30 ESEM FEG, Hillsboro, OR) and tapping mode atomic force microscopy (AFM, Dimension 2000 or Bioscope II, Veeco Metrology Inc., Santa Barbara, CA) were used to characterize the physical properties of the NCs. Silicon probes (RTESP, Veeco Metrology, Inc.) with spring constants of 20−80 N/m were used for AFM imaging.

Finite Element Modeling. We used the finite element method (FEM) to calculate the response of different NC samples to external electromagnetic excitation. All FEM simulations are performed with the commercial software COMSOL 3.5a using scattered harmonic propagation (radio frequency module). The refractive index of the substrate beneath the NCs is chosen to match the glass substrate used in the experiment (n = 2.04). A perfectly matched layer (PML) is used as an absorbing layer to simulate the infinite space surrounding the nanoparticles. The PML is placed far enough to accommodate the largest value of the nanoparticle optical extinction cross section. The Au material is modeled using experimentally measured dielectric data.[39] Linear interpolation is used to predict the dielectric properties between the data points. A simple geometrical model is used to represent the NCs of small/large aspect ratio. The model is built according to the fabrication steps as a wide block of Au of 40 nm

height (the same as experimentally deposited Au thickness). To resemble the PS shadow, a cylinder of 410 nm diameter (the PS template diameter), tilted by the azimuthal deposition angle, is used to remove a tilted elliptical hole in the Au film. A vertical cylinder of 410 nm diameter is used to model the vertical etching by removing the Au film parts outside this cylinder. The final geometry has a realistic NC shape, with a trapezoidal cross section of maximum area at the center and minimum at the tips. The silicon layers are modeled such that silicon covers the NC and the surrounding area. The silicon material is modeled using experimentally measured dielectric data, which is almost frequency independent in the frequency range of interest ($n = 3.46$).

The optical extinction cross section is calculated by adding the optical absorption and the optical scattering together.[40] The optical absorption essentially is the thermal energy absorbed inside the metallic particle (calculated directly by the solver), multiplied by a factor incorporating the surrounding medium optical properties. The optical scattering is calculated using the far-field transformation. The far-field components are calculated directly by the solver on top of a defined far-field spherical monitor surface. The calculated far-field energy is normalized against the far-field monitor surface area to obtain the scattering cross section.

Acknowledgment. J.S.S.-P. gratefully acknowledges support from a National Science Foundation Career Award (0844764), and P.N. and T.A. acknowledge support from the Robert A. Welch Foundation under Grant C-1222.

REFERENCES AND NOTES

1. Willets, K. A.; Van Duyne, R. P. Localized Surface Plasmon Resonance Spectroscopy and Sensing. *Annu. Rev. Phys. Chem.* **2007**, *58*, 267–297.
2. Maier, S. A.; Brongersma, M. L.; Kik, P. G.; Meltzer, S.; Requicha, A. A. G.; Atwater, H. A. Plasmonics—A Route to Nanoscale Optical Devices. *Adv. Mater.* **2001**, *13*, 1501–1505.
3. Atwater, H. A. The Promise of Plasmonics. *Sci. Am.* **2007**, *296*, 56–63.
4. Rosi, N. L.; Mirkin, C. A. Nanostructures in Biodiagnostics. *Chem. Rev.* **2005**, *105*, 1547–1562.
5. Aubry, A.; Lei, D. Y.; Fernández-Domínguez, A. I.; Sonnefraud, Y.; Maier, S. A.; Pendry, J. B. Plasmonic Light-Harvesting Devices over the Whole Visible Spectrum. *Nano Lett.* **2010**, *10*, 2574–2579.
6. Baker, G. A.; Moore, D. S. Progress in Plasmonic Engineering of Surface-Enhanced Raman-Scattering Substrates toward Ultra-Trace Analysis. *Anal. Bioanal. Chem.* **2005**, *382*, 1751–1770.
7. Zhang, J.; Malicka, J.; Gryczynski, I.; Lakowicz, J. R. Surface-Enhanced Fluorescence of Fluorescein-Labeled Oligonucleotides Capped on Silver Nanoparticles. *J. Phys. Chem. B* **2005**, *109*, 7643–7648.
8. Hirsch, L. R.; Gobin, A. M.; Lowery, A. R.; Tam, F.; Drezek, R. A.; Halas, N. J.; West, J. L. Metal Nanoshells. *Ann. Biomed. Eng.* **2006**, *34*, 15–22.
9. Haes, A. J.; Chang, L.; Klein, W. L.; Van Duyne, R. P. Detection of a Biomarker for Alzheimer's Disease from Synthetic and Clinical Samples Using a Nanoscale Optical Biosensor. *J. Am. Chem. Soc.* **2005**, *127*, 2264–2271.
10. Quinten, M.; Leitner, A.; Krenn, J. R.; Aussenegg, F. R. Electromagnetic Energy Transport *via* Linear Chains of Silver Nanoparticles. *Opt. Lett.* **1998**, *23*, 1331–1333.
11. Zia, R.; Schuller, J. A.; Chandran, A.; Brongersma, M. L. Plasmonics: The Next Chip-Scale Technology. *Mater. Today* **2006**, *9*, 20–27.
12. Maier, S. A.; Friedman, M. D.; Barclay, P. E.; Painter, O. Experimental Demonstration of Fiber-Accessible Metal Nanoparticle Plasmon Waveguides for Planar Energy Guiding and Sensing. *Appl. Phys. Lett.* **2005**, *86*, 071103.
13. Klar, T.; Perner, M.; Grosse, S.; von Plessen, G.; Spirkl, W.; Feldmann, J. Surface-Plasmon Resonances in Single Metallic Nanoparticles. *Phys. Rev. Lett.* **1998**, *80*, 4249–4252.
14. Kottmann, J. P.; Martin, O. J. F.; Smith, D. R.; Schultz, S. Non-regularly Shaped Plasmon Resonant Nanoparticle as Localized Light Source for Near-Field Microscopy. *J. Microsc.* **2001**, *202*, 60–65.
15. Kundu, J.; Le, F.; Nordlander, P.; Halas, N. J. Surface Enhanced Infrared Absorption (SEIRA) Spectroscopy on Nanoshell Aggregate Substrates. *Chem. Phys. Lett.* **2008**, *452*, 115–119.
16. Hao, E.; Schatz, G. C. Electromagnetic Fields around Silver Nanoparticles and Dimers. *J. Chem. Phys.* **2004**, *120*, 357–366.
17. Maier, S. A.; Kik, P. G.; Atwater, H. A. Observation of Coupled Plasmon−Polariton Modes in Au Nanoparticle Chain Waveguides of Different Lengths: Estimation of Waveguide Loss. *Appl. Phys. Lett.* **2002**, *81*, 1714–1716.
18. Haes, A. J.; Zou, S. L.; Schatz, G. C.; Van Duyne, R. P. A Nanoscale Optical Biosensor: The Long Range Distance Dependence of the Localized Surface Plasmon Resonance of Noble Metal Nanoparticles. *J. Phys. Chem. B* **2004**, *108*, 109–116.
19. Haynes, C. L.; Van Duyne, R. P. Plasmon-Sampled Surface-Enhanced Raman Excitation Spectroscopy. *J. Phys. Chem. B* **2003**, *107*, 7426–7433.
20. Haes, A. J.; Zou, S. L.; Schatz, G. C.; Van Duyne, R. P. Nanoscale Optical Biosensor: Short Range Distance Dependence of the Localized Surface Plasmon Resonance of Noble Metal Nanoparticles. *J. Phys. Chem. B* **2004**, *108*, 6961–6968.
21. Whitney, A. V.; Elam, J. W.; Zou, S. L.; Zinovev, A. V.; Stair, P. C.; Schatz, G. C.; Van Duyne, R. P. Localized Surface Plasmon Resonance Nanosensor: A High-Resolution Distance-Dependence Study Using Atomic Layer Deposition. *J. Phys. Chem. B* **2005**, *109*, 20522–20528.
22. Larsson, E. M.; Alegret, J.; Kall, M.; Sutherland, D. S. Sensing Characteristics of NIR Localized Surface Plasmon Resonances in Gold Nanorings for Application as Ultrasensitive Biosensors. *Nano Lett.* **2007**, *7*, 1256–1263.
23. Jung, L. S.; Campbell, C. T.; Chinowsky, T. M.; Mar, M. N.; Yee, S. S. Quantitative Interpretation of the Response of Surface Plasmon Resonance Sensors to Adsorbed Films. *Langmuir* **1998**, *14*, 5636–5648.
24. Frutos, A. G.; Corn, R. M. SPR of Ultrathin Organic Films. *Anal. Chem.* **1998**, *70*, 449A–455A.
25. Malinsky, M. D.; Kelley, K. L.; Schatz, G. C.; Van Duyne, R. P. Chain Length Dependence and Sensing Capabilities of the Localized Surface Plasmon Resonance of Silver Nanoparticles Chemically Modified with Alkanethiol Self-Assembled Monolayers. *J. Am. Chem. Soc.* **2001**, *123*, 1471–1482.
26. Phillips, K. S.; Han, J.-H.; Martinez, M.; Wang, Z.; Carter, D.; Cheng, Q. Nanoscale Glassification of Gold Substrates for Surface Plasmon Resonance Analysis of Protein Toxins with Supported Lipid Membranes. *Anal. Chem.* **2006**, *78*, 596–603.
27. Shumaker-Parry, J. S.; Rochholz, H.; Kreiter, M. Fabrication of Crescent-Shaped Optical Antennas. *Adv. Mater.* **2005**, *17*, 2131–2134.
28. Bukasov, R.; Shumaker-Parry, J. S. Highly-Tunable Infrared Extinction Properties of Gold Nanocrescents. *Nano Lett.* **2007**, *7*, 1113–1118.
29. Rochholz, H.; Bocchio, N.; Kreiter, M. Tuning Resonances on Crescent-Shaped Noble-Metal Nanoparticles. *New J. Phys.* **2007**, *9*, 53.
30. Ross, B. M.; Lee, L. P. Plasmon Tuning and Local Field Enhancement Maximization of the Nanocrescent. *Nanotechnology* **2008**, *19*, 275201-1.
31. Bukasov, R.; Shumaker-Parry, J. Silver Nanocrescents with Infrared Plasmonic Properties as Tunable Substrates for Surface Enhanced Infrared Absorption Spectroscopy. *Anal. Chem.* **2009**, *81*, 4531–4535.
32. Bocchio, N. L.; Unger, A.; Alvarez, M.; Kreiter, M. Thin Layer Sensing with Multipolar Plasmonic Resonances. *J. Phys. Chem. C* **2008**, *112*, 14355–14359.
33. Masson, J.-F.; Ludovic, S. L. High Sensitivity of Plasmonic Microstructures near the Transition from Short-Range to

Propagating Surface Plasmon. *J. Phys. Chem. C* **2009**, *113*, 100052–10060.
34. Hao, E.; Schatz, G. C.; Hupp, J. T. Synthesis and Optical Properties of Anisotropic Metal Nanoparticles. *J. Fluoresc.* **2004**, *14*, 331–341.
35. Sherry, L. J.; Jin, R. C.; Mirkin, C. A.; Schatz, G. C.; Van Duyne, R. P. Localized Surface Plasmon Resonance Spectroscopy of Single Silver Triangular Nanoprisms. *Nano Lett.* **2006**, *6*, 2060–2065.
36. Haes, A. J.; Van Duyne, R. P. A Nanoscale Optical Biosensor: Sensitivity and Selectivity of an Approach Based on the Localized Surface Plasmon Resonance Spectroscopy of Triangular Silver Nanoparticles. *J. Am. Chem. Soc.* **2002**, *124*, 10596–10604.
37. Jain, P. K.; El-Sayed, M. A. Plasmonic Coupling in Noble Metal Nanostructures. *Chem. Phys. Lett.* **2010**, *487*, 153–164.
38. Nelson, K. E.; Gamble, L.; Jung, L. S.; Boeckl, M. S.; Naomi, E.; Golledge, S. L.; Sasaki, T.; Castner, D. G.; Campbell, C. T.; Stayton, P. S. Surface Characterization of Mixed Self-Assembled Monolayer Designed for Streptavidin Immobilization. *Langmuir* **2001**, *17*, 2807–2816.
39. Johnson, P. B.; Christy, R. W. Optical-Constants of Noble-Metals. *Phys. Rev. B* **1972**, *6*, 4370–4379.
40. Bohren, C. F.; Huffmann, R. D. *Absorption and Scattering of Light by Small Particles*; Wiley & Sons: New York, 1983.